The Journal of Immunology

RESEARCH ARTICLE | MARCH 15 2023

A Microphysiological Device to Model the Choriodecidual Interface Immune Status during Pregnancy

Lauren Richardson; ... et. al

J Immunol (2023) 210 (9): 1437–1446.
https://doi.org/10.4049/jimmunol.2200821

A Microphysiological Device to Model the Choriodecidual Interface Immune Status during Pregnancy

Lauren Richardson,* Enkhtuya Radnaa,* Ryan C. V. Lintao,*,† Rheanna Urrabaz-Garza,* Ruhi Maredia,‡ Arum Han,§,¶,‖ Jiaren Sun,# and Ramkumar Menon*

During human pregnancy the chorion (fetal) lines decidua (maternal) creating the feto–maternal interface. Despite their proximity, resident decidual immune cells remain quiescent during gestation and do not invade the chorion. Infection and infiltration of activated immune cells toward the chorion are often associated with preterm birth. However, the mechanisms that maintain choriodecidual immune homeostasis or compromise immune barrier functions remain unclear. To understand these processes, a two-chamber microphysiological system (MPS) was created to model the human choriodecidual immune interface under normal and infectious conditions in vitro. This MPS has outer (fetal chorion trophoblast cells) and inner chambers (maternal decidual + CD45$^+$ cells [70:30 ratio]) connected by microchannels. Decidual cells were treated with LPS to mimic maternal infection, followed by immunostaining for HLA-DR and HLA-G, immune panel screening by imaging cytometry by time of flight, and immune regulatory factors IL-8 and IL-10, soluble HLA-G, and progesterone (ELISA). LPS induced a proinflammatory phenotype in the decidua characterized by a decrease in HLA-DR and an increase in IL-8 compared with controls. LPS treatment increased the influx of immune cells into the chorion, indicative of chorionitis. Cytometry by time of flight characterized immune cells in both chambers as active NK cells and neutrophils, with a decrease in the abundance of nonproinflammatory cytokine-producing NK cells and T cells. Conversely, chorion cells increased progesterone and soluble HLA-G production while maintaining HLA-G expression. These results highlight the utility of MPS to model choriodecidual immune cell infiltration and determine the complex maternal–fetal crosstalk to regulate immune balance during infection. ***The Journal of Immunology*****, 2023, 210: 1437–1446.**

Maintenance of human pregnancy requires immune tolerance at the feto–maternal interfaces (FMis) (1–4). A well-balanced system is ensured by a harmonious existence of feto–maternal immune cells, endocrine and paracrine mediators, and other mechanical factors (5–9). This balanced system is needed for fetoplacental and fetal membrane growth (10, 11). Parturition is an inflammatory process where disturbances at the FMi collapse immune balance, increase inflammatory activation, and exhibit a bidirectional influx of immune cells facilitated by cytokine and chemokine production (7). This is a natural and physiologic process required to deliver the fetus by activation of multitudes of quiescent uterine systems (12–14). However, disturbances to this system in response to various pregnancy-associated risk factors (e.g., intra-amniotic infection and inflammation) can prematurely cause immune intolerance in various intrauterine tissues, contributing to adverse pregnancy outcomes such as preterm premature rupture of the membranes and spontaneous preterm birth (15–20).

Past studies on the FMi have been primarily focused on the placental–decidual interface (21, 22). For example, extensive investigations on the interactive roles of immune cells in the decidua basalis have been conducted, and various immunoregulatory markers on extravillous trophoblast, cytotrophoblast, and syncytial trophoblast cells have been reported (23–26). However, another FMi, namely the fetal membrane–decidual interface or choriodecidual interface, has been not well studied despite the emerging importance of this interface on maintaining healthy pregnancy (5, 27, 28). In this

*Division of Basic and Translational Research, Department of Obstetrics and Gynecology, The University of Texas Medical Branch at Galveston, Galveston, TX; †Department of Biochemistry and Molecular Biology, College of Medicine, University of the Philippines Manila, Manila, Philippines; ‡John Sealy School of Medicine at Galveston, The University of Texas Medical Branch at Galveston, Galveston, TX; §Department of Electrical and Computer Engineering, Texas A&M University, College Station, TX; ¶Department of Biomedical Engineering, Texas A&M University, College Station, TX; ‖Department of Chemical Engineering, Texas A&M University, College Station, TX; and #Department of Microbiology & Immunology, The University of Texas Medical Branch at Galveston, Galveston, TX

ORCIDs: 0000-0001-8392-2833 (L.R.); 0000-0001-8142-8137 (E.R.); 0000-0001-7192-2377 (R.C.V.L.); 0000-0002-7682-0246 (R. Maredia); 0000-0002-9223-8301 (A.H.); 0000-0001-5084-4437 (J.S.); 0000-0001-9213-6105 (R. Menon).

Received for publication November 4, 2022. Accepted for publication February 23, 2023.

This work was supported by the Eunice Kennedy Shriver National Institute of Child Health and Human Development Grant R01HD100729-01S1 to R. Menon. L.R. is supported by an Institute of Human and Infections and Immunity pilot fund grant at The University of Texas Medical Branch at Galveston and by a research career development award (National Institute of Allergy and Infectious Diseases Grant K12HD052023: Building Interdisciplinary Research Careers in Women's Health Program; Berenson, PI) from the National Institutes of Health/Office of the Director, the National Institute of Allergy and Infectious Diseases, and the Eunice Kennedy Shriver National Institute of Child Health and Human Development. The content is solely the responsibility of the authors and does not necessarily represent the official views of the National Institutes of Health. R.C.V.L. is an MD-PhD in Molecular Medicine Program trainee supported by the Department of Science and Technology–Philippine Council for Health Research and Development.

Project ideas were conceived and funding was provided by R. Menon; R.U.-G., E.R., R. Maredia, R.C.V.L., and L.R. conducted the experiments; L.R. helped with data analysis and J.S. helped with the interpretation of immune cell phenotyping; L.R. and R. Menon prepared the manuscript; and A.H. reviewed the manuscript and contributed to chip design.

Address correspondence and reprint requests to Dr. Ramkumar Menon, Division of Basic Science and Translational Medicine, Department of Obstetrics & Gynecology, The University of Texas Medical Branch at Galveston, 301 University Boulevard, Galveston, TX 77555-1062. E-mail address: ra2menon@utmb.edu

The online version of this article contains supplemental material.

Abbreviations used in this article: CTC, chorion trophoblast cell; CyTOF, cytometry by time of flight; DEC, decidual cell; FMi, feto–maternal interface; hFM, human fetal membrane; IRB, Institutional Review Board; MPS, microphysiological system; P4, progesterone; PDMS, polydimethylsiloxane; sHLA-G, soluble HLA-G; *t*-SNE, *t*-distributed stochastic neighbor embedding.

study, chorionic trophoblast cells of the amniochorionic membrane (i.e., fetal membrane) line the decidua parietalis to form the choriodecidual interface (29–32). Compared to the placental interface, this interface forms the innermost uterine structure, lines the entire intrauterine cavity, and covers various uterine tissues (e.g., cervix, placenta, and myometrium) (33). Similar to the decidua basalis, the decidua parietalis region also harbors immune cells (~30%) (3, 14, 34), and decidual cells (DECs) also demonstrate immune cell-like properties (e.g., Ag-presenting histocompatibility Ag HLA-DR) (35). Although the lineage of trophoblast cells in the placenta and fetal membranes may be the same, chorion trophoblasts are distinct in their location, structure, and function compared with placental cytotrophoblast cells. This reiterates the notion that the fetal membrane, and the chorion in particular, is not just a mere extension of the placenta.

Recent data from our laboratory indicate that chorion trophoblast cells are a rich source of the pregnancy maintenance hormone progesterone (P4) and anti-inflammatory cytokine IL-10, and they express immunoregulatory HLA-G that does not change regardless of the pregnancy condition (preterm versus term or term labor versus term not in labor) (36). Infection and inflammation-induced stress on chorion trophoblasts are often associated with high levels of IL-8 and TNF-α production, indicating them as biomarkers of chorionic cell stress. HLA-G presentation as well as P4, IL-10, and soluble HLA-G (sHLA-G) production by chorion trophoblasts are likely the armories used by the fetal membrane to shield against the invasion of decidual immune cells. Thus, the choriodecidual interface is thought to function as a major barrier or "great wall" during pregnancy, and any compromise to this barrier function can be detrimental to pregnancy. Therefore, a better understanding of this interface is needed to elucidate its normal functions during pregnancy and how a compromise to this interface can lead to intra-amniotic invasion of pathogens and other risk factors leading to the fetal inflammatory response.

However, studies of the FMi are difficult, as obtaining these tissues to understand their functional contributions during pregnancy and parturition is impractical. Tissues obtained after delivery, either after preterm birth or term gestations, are compromised in their architectural and functional properties confounded by various factors that are beyond controllable levels. Animal models are also limited, as the structure and function of the fetal membrane–decidual region in these models are different from what is seen in human pregnancy (37). These limitations led us to develop a microphysiological system (MPS) (e.g., organ-on-chip or tissue chip) of the FMi using chorion trophoblast, decidual, and resident decidual primary immune cells to study the choriodecidual interface that simulates these organs in vitro while maintaining their interactions as seen in vivo. We have then used this system to study the properties of amnion epithelial and mesenchymal cells of the fetal membranes (38). In that study, we showed that intercellular interactions, cellular transitions, and migration can be monitored using this device (38). Despite these successes, these FMi MPS models are still limited, as they lack immune cells, which is an integral component and contributes unique properties to this interface. In this study, we modified our previously developed two-chamber, interconnected, amnion membrane MPS model to mimic the choriodecidual immune interface, where the interconnected microchannels allow for the passage of cells and molecules across the cell barriers when the barrier is compromised. We first determined the utility of this model in testing the biological and biochemical properties of the choriodecidual immune interface in normal conditions. In addition, we modeled infection-associated (e.g., LPS stimulation) functional changes to the chorion barrier of this interface using this model.

Materials and Methods

Institutional Review Board approval

This study protocol is approved by the Institutional Review Board (IRB) at The University of Texas Medical Branch (UTMB) at Galveston, TX, as an exempt protocol to use of discarded placenta after normal term cesarean deliveries (UTMB no. 11-251). No subject recruitment or consent was required for this study.

Clinical samples

Inclusion criteria. Criteria for inclusion were normal repeat or nulliparous subjects and scheduled cesarean term deliveries from women with no pregnancy-related complications who were not in labor. We could not extract any additional clinical or demographic data, as our IRB protocol is restricted to discarded human specimens (placenta) only. Therefore, any additional data collection will require identifiers, and this is one of the limitation of these studies.

Exclusion criteria. Term labor vaginal deliveries ($>39^{0/7}$ wk) were excluded. Subjects with multiple gestations, placenta previa, fetal anomalies, and/or medical or surgeries (intervention for clinical conditions that are not linked to pregnancy) during pregnancy were excluded. Severe cases of preeclampsia or persistent symptoms (headache, vision changes, right upper quadrant pain) or abnormal laboratory findings (thrombocytopenia, repeated abnormal liver function tests, creatinine doubling or >1.2, or HELLP [hemolysis, elevated liver enzymes, low platelet count] syndrome) or clinical findings (pulmonary edema or eclampsia) were excluded. Subjects who had any surgical procedures during pregnancy or who were treated for hypertension, preterm labor, or for suspected clinical chorioamnionitis (reports on foul-smelling vaginal discharge, high levels of C-reactive protein, fetal tachycardia), positive group B *Streptococcus* screening or diagnosis of bacterial vaginosis, behavioral issues (cigarette smoking, drug or alcohol abuse), and delivered at term were excluded from the control groups.

Primary immune cell isolation from the decidua parietalis. Graphical representation of this protocol can be found in Supplemental Fig. 1. $CD45^+$ immune cells isolated from the decidua parietalis are maternal immune cells (39). Prior to these chip experiments, primary immune cells isolated from the decidua parietalis were screed by flow cytometry to determine the subpopulations of $CD45^+$ leukocytes present at the FMi (e.g., ~66% T cells, ~13% NK cells, ~4% macrophages, ~4% B cells, ~1.2% neutrophils). From the viable cell population, $CD45^+$ cells made up 87%, while the remaining 13% is thought to be resident DECs. The fetal membrane was cut from the placenta and the amnion and chorion were manually separated ($n = 6$ biological replicates). The chorion layer was placed into a sterile petri dish and decidua parietalis along with blood clots was gently collected using a cell scraper. The scraped decidua tissue was then placed in a sterile petri dish with HBSS and transferred into a biosafety cabinet. The tissue was then strained through a 250-μm metal sieve fitted with no. 60 mesh size and washed twice with HBSS. The tissue was collected from the strainer and digested at 37°C for 20 min with rotation in a solution containing 10% FBS, 2 mg/ml collagenase 2, 0.1 mg/ml soybean trypsin inhibitor, 0.15 mg/ml DNase 1, and 1 mg/ml BSA in HBSS. Once incubation was completed, the tissue was strained through the 250-μm sieve with no. 60 mesh size, and the strained solution was neutralized with equal volume complete media (RPMI 1640, 10% FBS, and 1% penicillin-streptomycin). The cell solution was then centrifuged at 420 × *g*, 4°C, 11 min. The pelleted cells were resuspended in 2% washing solution (RPMI 1640, 2% FBS, and 1% penicillin-streptomycin) and centrifuged at 420 × *g*, 4°C, 11 min. The supernatant was removed and the cell pellet was resuspended in RBC lysis solution and incubated for 5 min at room temperature. The solution was then centrifuged at 420 × *g*, 4°C, 11 min. the cell pellet was washed with 2% washing solution, passed through a 100-μm strainer, and centrifuged at 420 × *g*, 4°C, 11 min. The pellet was then resuspended in FACS buffer (Dulbecco's PBS, 5% FBS), and leukocytes were enriched from a total population of DECs by density gradient centrifugation. The cell suspension was gently overlaid on top of an equal volume Ficoll (density 1.077 g/ml + 0.001 g/ml) in a 15-ml centrifuge tube, ensuring the two layers did not mix. The tube was then centrifuged at 500 × *g* for 30 min without brake. Leukocytes were collected from the interface between the Ficoll and FACS buffer and placed in a clean tube. Using this isolation strategy, low-density neutrophils, contained within the mononuclear cell layer, will be included within the cultured cell populations. Three times the volume of FACS buffer was added to the tube and the solution was centrifuged at 420 × *g*, 4°C, 11 min. The pelleted cells were resuspended in 2% washing solution and spun again at 420 × *g*, 4°C, 11 min. The supernatant was removed, and the final cell pellet was resuspended in complete RPMI 1640 media. Cells were counted, placed in an appropriate culture vessel with complete media, and placed in 37°C incubators with 5% CO_2.

Human chorion and DEC cultures

Prior to conducting experiments, primary fetal membrane chorion cells and maternal DECs from different donors were isolated and immortalized to obtain stable cell lines to be used on-chip. The same cell lines were used for all experiments. The decidua parietalis and human fetal membrane (hFM) cells (hFM_DECs) were isolated from placenta collected from women undergoing elective cesarean delivery at term who were not in labor (as described in Refs. 40–42), and IRB approval was no. 16-0058, January 2020. Immortalized cells have been validated against primary cells (43). Human chorion trophoblast cells (hFM_CTCs) were cultured in DMEM/F12 supplemented with 0.20% FBS, 0.1 mM 2-ME, 0.5% penicillin-streptomycin, 0.3% BSA, 1× insulin-tranferrin-selenium-ethanolamine, 5 μM Y27632, 2 μM CHIR99021, 0.5 μM A83-01, 1.5 μg/ml L-ascorbic acid, 50 ng/ml epithelial growth factor, and 0.08 mM valproic acid (40). All cells were grown at 37°C and 5% CO_2 until they reached 80–90% confluence. hFM_DECs were cultured in DMEM/F12 (Mediatech, Manassas, VA) supplemented with 10% FBS, 10% penicillin-streptomycin (Mediatech), and 10% amphotericin B (Sigma-Aldrich, St. Louis, MO) at 37°C and 5% CO_2 for 10 min. Cells under passage 20 were used for experiments.

Microfluidic MPS designs

The microfabrication procedure is similar to that previously outlined for the amnion membrane MPS (38) (Supplemental Fig. 2A) and the cervix epithelial MPS (44). To summarize, a two-step photolithography process was conducted using a photosensitive epoxy (SU-8; MicroChem, Westborough, MA) to fabricate the master mold, forming the first microchannel layer (24 channels; 5 μm high, 600 μm long, 30 μm wide) and the second cell culture chamber layer (500 μm high). The master mold was then coated with (tridecafluoro-1,1,2,2-tetrahydrooctyl)trichlorosilane (United Chemical Technologies, Bristol, PA) to facilitate polydimethylsiloxane (PDMS) release from the master mold after replication. A soft lithography technique was used to make the MPSs out of PDMS. PDMS devices were replicated from the master mold by pouring PDMS prepolymer (10:1 mixture, Sylgard 184; DowDuPont, Midland, MI) onto the mold, followed by curing at 85°C for 45–60 min. To hold the culture medium, reservoirs were punched out from this PDMS layer using a 4-mm-diameter biopsy punch. This PDMS layer was treated with oxygen plasma (Harrick Plasma, Ithaca, NY) for 90 s to improve the bonding of the PDMS layer onto the glass substrate and to also make the device hydrophilic for easy cell and culture medium loading, followed by bonding onto a glass substrate (22 × 22 mm). A single device (2 × 2 cm) fits within a well of a six-well culture plate. Prior to use, MPSs were washed with 70% ethanol for 10 min to sterilize, then washed three times with 1× PBS. The microchannels were left open to allow for cell–cell interaction between the chorion and decidua cultures.

Cell seeding and treatment in the MPS

After sterilization, the devices were washed three times with 1× PBS before cell seeding. hFM_CTCs were seeded in the outer chamber (100,000 cells) and hFM_DECs and $CD45^+$ leukocytes were mixed and loaded into the inner chamber (28,000 hFM_DECs + 12,000 $CD45^+$ cells). Seeding densities were determined through previous cell loading titrations and based on cell ratios seen in in vivo ratios. A total volume of 200 μl of medium was added to the outer chamber and 80 μl of medium to the inner chamber (RPMI 1640, 10% FBS, 1% penicillin-streptomycin) to create uniform hydraulic pressure. The MPSs were incubated at 37°C with 5% CO_2 overnight to allow for cell attachment, and then the culture medium was changed for the center chambers. The inner chamber was cultured with either standard culture medium (control) or 100 ng/ml LPS (45) to model ascending infection. After 24 h, media from both chambers were extracted for further testing and cells underwent endpoint immunostaining.

Microscopy

Bright-field microscopy. Images were captured using a Nikon Eclipse TS100 microscope (×4, ×10, ×20 magnification) (Nikon). Three regions of interest per condition were used to determine the overall cell morphology.

Fluorescence microscopy. A Keyence all-in-one fluorescence BZ-X810 microscope (×4, ×10, and ×40 magnification) was used to determine $CD45^+$ leukocyte migration and histocompatibility Ag (HLA) expression. Stitched images, covering half of the MPS, were analyzed for $CD45^+$ leukocyte migration (~2400 × 5000 pixels) as noted by $CD45^+$ punctate cells in the outer chorion chamber. The total number of $CD45^+$ cells in the outer chamber was counted manually using the ImageJ cell counter feature. The number of $CD45^+$ cells in the inner chamber was not quantified or used as a denominator to normalize images, and therefore this quantification method is semiquantitative and provides absolute values for analysis. Three representative regions of each chamber were imaged per chip for the quantification of HLAs (intensity analysis via ImageJ).

Live cell imaging. To determine the ability of immune cells to actively cross through the microchannels, $CD45^+$ leukocytes were stained using NucBlue Live Cell ReadyProbes (R37605; Invitrogen) or CellLight histone 2B-FITC (C10595; Invitrogen). Manufacture protocols were followed for the live staining kits. MPSs were seeded as previously described and incubated within the CO_2 chamber (KIW chamber) of the Keyence BZ-X810 microscope. Green or blue fluorescently labeled $CD45^+$ leukocytes were monitored for 12 h.

Immunocytochemistry staining

Immunocytochemical staining for CD45 (Abcam, ab30470; 1:200), vimentin (Abcam, ab92547; 1:500), cytokeratin-18 (Abcam, ab668; 1:800), HLA-G (Abcam, ab52455; 1:200), and HLA-DR (Abcam, ab929511; 1:50) were used to monitor cell types and document their immune regulatory status. Abs were titrated to determine appropriate dilutions to ensure specific and uniform staining. After 24 h, cells were fixed with 4% paraformaldehyde, permeabilized with 0.5% Triton X-100, and blocked with 3% BSA in 1× PBS, before incubation with primary Abs overnight. Cells were washed three times in 1× PBS and then incubated with species-specific secondary Abs (1:1000) for 1 h. The MPSs were washed with 1× PBS and then treated with NucBlue Fixed ReadyProbes reagent (R37606; Thermo Fisher Scientific, Waltham, MA) to stain the nucleus. Primary and secondary concentrations were validated based on previous chip-based studies.

Cell viability

To determine immune cell viability after primary isolation, immune cells were cultured with or without DECs for 24 or 48 h on glass coverslips. Before fixation, media were removed from all cell culture chambers, and each chamber was washed with 1× PBS. A combination of conjugated live and dead cell staining Abs, calcein-AM (for live cells; green; 4 mM) and ethidium homodimer-1 (for dead cells; red; 2 mM) (Thermo Fisher Scientific, L3224), were added into the cell culture chambers and incubated for 30 min in the dark with gentle rocking. The chambers were then washed with PBS, treated with NucBlue Live ReadyProbes reagent (Thermo Fisher Scientific), and imaged as described above. Senescent cells were identified using a histochemical staining kit (ab65351, Abcam), with blue cells visualized (senescence associated β-galactosidase) by light microscopy at 48 h after immune cells were cultured with DECs. Laser settings, brightness, contrast, and collection settings were all uniform for all images collected.

Histology

Human choriodecidual interface biopsies were fixed in 4% paraformaldehyde for 48 h and embedded in paraffin. Sections were cut at 5-μm thickness and adhered to a positively charged slide and attached by keeping them at 57°C for 45 min. Slides were deparaffinized using xylene and rehydrated with 100% alcohol, 95% alcohol, and normal saline (pH 7.4), then stained. Three images for each category were taken at ×10 and ×40 magnification. Anti-human Ab CD45 (ab30470, Abcam) was used for immunohistochemistry.

Imaging mass cytometry analysis

Panel design. Imaging mass cytometry Ab panel was designed to determine immune subphenotypes and their activation status (see Tables I, II).

Abs used. All preconjugated and commercially available Abs were purchased from the Flow Cytometry and Cellular Imaging Core Facility, The University of Texas MD Anderson Cancer Center (Table II). All metal-tagged Abs were stored at 4°C. Ab concentration and specificity were evaluated by visual inspection of the imaging mass cytometry images of control versus LPS-treated $CD45^+$ primary immune cells in the inner chamber of the MPS device using MCD Viewer software (Fluidigm). The resulting staining patterns were compared with the control results presented by various publications (BenchSci) and the various Ab vendors.

Sample preparation and imaging mass cytometry staining. After 24 h of control or LPS treatment, the medium from the devices was removed. All staining procedures were conducted inside the organ-on-a-chip devices. Then, cells were treated with a Fc receptor block (BioLegend, San Diego, CA, 101302) for 10 min at room temperature. Then, a surface Ab mixture (CD3, CD4, CD25, CD45, CD8a, HLA-DR, CD11c, CD68, CD80, CD19, CD66b, CD206/MMR, CD56, CD86, CD16) was added and incubated for 30 min at room temperature. Cells were then washed with Maxpar PBS (Fluidigm, San Francisco, CA, 201058) for 5 min at room temperature. Cells were fixed with 4% paraformaldehyde in PBS for 20 min at room temperature. After washing with Maxpar PBS (Fluidigm) for 5 min, an intracellular Ab mixture (cytokeratin, vimentin, IFN-γ, IL-17A, IL-4) was added to the cells for 1 h at room temperature. Cells were then washed three times with

Maxpar PBS (Fluidigm) for 5 min and incubated with 125 nM intercalator-Ir (Fluidigm, 201192A) for 1 h at room temperature. Lastly, cells were washed three times with Maxpar PBS (Fluidigm) for 5 min and once with Maxpar H_2O (Fluidigm, 201069). After staining was complete, the PDMS chamber was removed, and the adherent stained cells that remained on the glass side were air dried for Hyperion ablation.

Imaging mass cytometry ablation. Images were acquired using a Hyperion mass cytometry system (Fluidigm). Laser ablation of the stained slides was conducted at the Flow Cytometry and Cellular Imaging Core Facility, The University of Texas MD Anderson Cancer Center (North Campus). The Hyperion was autotuned using a three-element tuning slide (Fluidigm) according to the tuning protocol provided by the imaging system user guide (Fluidigm). Regions of interest were selected based on a prescanned stitched slide images that selected three regions of interest that equaled 1 × 1 mm per slide section in the inner and outer chamber. Three biological replicates were imaged for each category of the groups (control or LPS treated). Ablation was conducted at 200 Hz and raw images were collected.

Imaging mass cytometry data analysis. Raw data were exported as MCD files and visualized using the Fluidigm MCD Viewer (https://www.fluidigm.com/products-services/software). Individual image files for each stain and region of interest were exported from the MCD Viewer as a 16-bit multilayer TIFF file. CellProfiler (https://cellprofiler.org/) was used to conduct cell segmentation and generate a cell mask. A pipeline was built focusing on the CD45 stain (Fluidigm, 3089003B; 89Y labeled, dilution factor 1:12) as the primary object (5–20 pixels) and 3 pixels outside the primary object the cytoplasm mask was created. All files were run through this pipeline and cell masks were generated for each tissue and region of interest. The TIFF files and cell masks were loaded into histoCAT (https://bodenmillergroup.github.io/histoCAT/) for phenotypic analysis. Each condition (i.e., outer+inner chamber of control devices or outer+inner chamber of LPS-treated devices; three regions of interest for three replicates) was analyzed together in the same pipeline. All marker expression data per category was visualized as a *t*-distributed stochastic neighbor embedding (*t*-SNE) plot. Phenograph analysis was conducted using standard histoCAT settings to generate unique cell clusters from control or LPS-treated chips. Cluster identification was achieved using the generated heatmaps for Ab intensity. Clusters of interest were determined when they met the following criteria: 1) contain at least 0.1 intensity of nuclear Ab expression, 2) targets that were below the threshold for clearly determining the identity, 3) did not contain at least 0.1 intensity of CD45 Ab expression, and 4) were dominated for vimentin or cytokeratin (markers of decidua and chorion cells). To identify the subphenotype of immune cells in each cluster, markers were analyzed that contained an expression level of 1 on the heatmap (i.e., highest expression). When more than one immune-specific marker met all the above criteria, raw data were analyzed to determine the dominant cell type in the cluster (Supplemental Fig. 3). Immune cells were deemed activated when they expressed proinflammatory cytokines (i.e., IL-4, IL-17a, IFN-γ) over the value 1.

Multiplex assays for inflammatory cytokine marker analyses using Luminex

To analyze changes in inflammatory mediators, IL-8, IL-10, GM-CSF, and TNF-α were analyzed from the cell supernatants in the MPSs after treatments. Supernatants were collected from the reservoirs of the devices using a pipette after 24 h. Standard curves were developed with duplicate samples of known quantities of recombinant proteins that were provided by the manufacturer. Sample concentrations were determined by relating the fluorescence values that were obtained to the standard curve by linear regression analysis.

ELISAs

Media from both chambers were collected to measure the amounts of P4 and sHLA-G that were secreted in the culture. To measure P4, a competitive ELISA (Invitrogen, EIAP4C21) was used by adding a competitive Ab after the addition of a secondary Ab following the manufacturer's instructions. sHLA-G was measured with an Enzo sHLA-G ELISA kit (ALX-850-309-KI01). Standard curves were developed with recombinant protein samples of known quantities. Sample concentrations were determined by correlating the sample absorbance to the standard curve by linear regression analysis.

Statistical analyses

All data were analyzed using the Prism 7 software (GraphPad Software, La Jolla, CA). A Student *t* test was used to compare results with two means.

Results

Utilization of a two-chamber MPS device to model the choriodecidual immune interface

To model the human choriodecidual immune interface (Supplemental Fig. 1A), a device design the same as a previously reported two-chamber MPS device (37, 44, 46) was used. The MPS is comprised of two concentric circular chambers connected through arrays of 24 microfluidic channels (Fig. 1A). The inner chamber in green represents the maternal decidual compartment whereas the outer chamber in purple represents the fetal chorion layer, therefore modeling the choriodecidual interface on-chip. Immortalized DECs (hFM_DECs) and primary fetal membrane-derived $CD45^+$ leukocytes (Supplemental Fig. 1B, 2B, 2C) were mixed at a 70:30 ratio and loaded into the inner chamber, whereas immortalized CTCs (hFM_CTC) were loaded into the outer chamber. Cells cocultured for 24 h maintained their respective morphologies and cell-specific markers (i.e., hFM_DECs, elongated $vimentin^+$ cells; leukocytes, small circular $CD45^+$ cells; hFM_CTCs, cuboidal $DAPI^+$ cells) (Fig. 1B). Owing to the microchannel height, hFM_DECs and hFM_CTCs loaded into each culture chamber remain separated in their respective chambers but still allow cell–cell interaction and migration (white arrows) through the microchannels (Fig. 1B).

Maternal infection induces changes in immune status at the choriodecidual immune interface

To determine the effect of maternal infection and infectious inflammation at the choriodecidual immune interface, 100 ng/ml LPS (45) was added to the inner hFM_DEC chamber of the MPS device, followed by analyzing the immunoregulatory Ags and immune cell migration after 24 h. Analysis of Ags that regulate immune function at the FMi was conducted using fluorescence microscopy. Expression of HLA-DR and HLA-G were analyzed in the hFM_DECs and hFM_CTCs on-chip, respectively. LPS treatment induced a significant reduction of hFM_DEC HLA-DR expression (green) ($p < 0.0001$), whereas it did not affect hFM_CTC HLA-G expression (red)

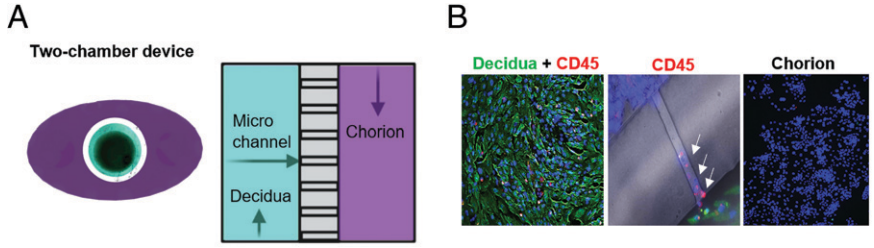

FIGURE 1. Establishment of a two-chamber choriodecidual immune interface model. (**A**) Dye-filled two-chamber polydimethylsiloxane (PDMS) device used to model the choriodecidual immune interface. The outer chamber was filled with purple dye and the inner chamber was filled with green dye. An array of microchannels connects the two chambers. (**B**) Representative fluorescent images of vimentin-positive decidual cells (green) and CD45-positive leukocytes in the inner chamber (red). Migratory leukocytes were identified by their CD45 staining within microchannels (white arrows). Chorion cells in the outer chamber were only stained with DAPI (blue) (original magnification ×10).

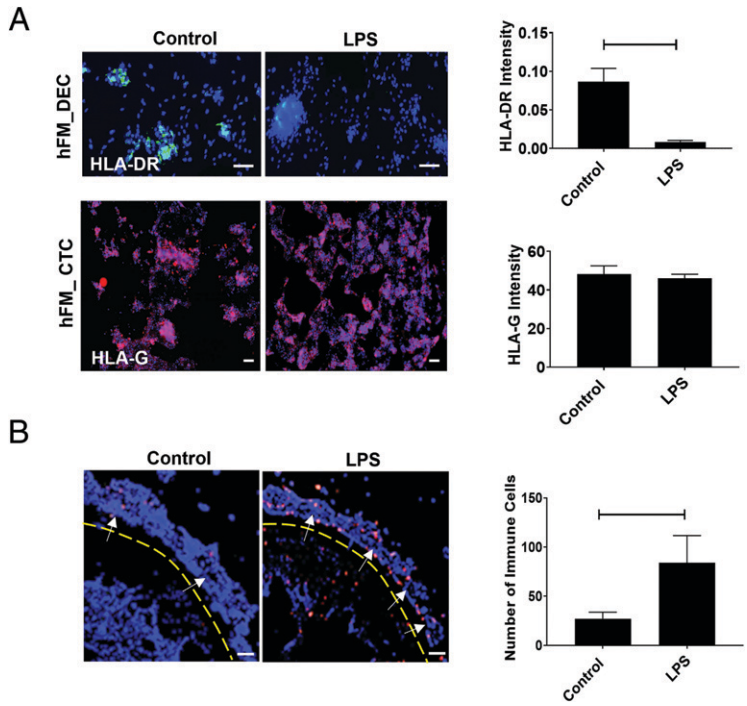

FIGURE 2. Immune status changes at the choriodecidual interface. (**A**) Representative fluorescent images of HLA-DR$^+$ decidual cells (green) and HLA-G$^+$ chorion cells in the inner chamber (red). LPS treatment induced a significant decrease in HLA-DR expression in the decidua ($p < 0.0001$), whereas HLA-G expression did not change in chorion cells. DAPI is in blue. Representative images (original magnification, ×10) are shown for $n = 6$ with three regions imaged per device. Images have been cropped to highlight marker staining. Graphs show mean ± SEM values. Scale bars, 100 μm. (**B**) Fluorescence microscopy images of CD45$^+$ (red) cell migration within the MPS device. Migrating cells were localized by CD45 and blue nuclear stain outside the inner chamber (yellow dashed circle). White arrows show the direction of cell migration. Bar graphs show values expressed as the number of migrated cells in devices with or without maternal LPS treatment. LPS induced a significant amount of cell migration into the outer chamber ($p = 0.03$). Representative images are shown for $n = 6$. Images have been cropped to focus on the microchannel interface. Graphs show mean ± SEM values. Scale bars, 100 μm.

compared with the controls (Fig. 2A). To determine the effect of maternal infection on promoting immune cell migration across the choriodecidual interface, immune cells on-chip were fluorescently stained for CD45 (red) and the absolute number of adherent immune cells in the outer chamber was quantified. Obtaining a relative count of immune cells is a limitation of this model, as it is easy to remove nonadherent or semiadherent immune cells after media collection in the inner chamber, providing inaccurate numbers to act as the denominator of a relative value. This is a limitation of this approach. Resident hFM_DEC immune cells migrated through microchannels (see yellow lines, Fig. 2B) into the CTC chamber within 6 h (Supplemental Fig. 2B, 2C), and migration plateaued after 24 h. LPS treatment induced a significant amount of immune cell migration ($p = 0.03$) after 24 h compared with control devices (Fig. 2B). These data suggest that maternal infection can induce hFM_DEC immune cell migration into the fetal hFM_CTC layer, and that our MPS model is ideal in determining their migratory properties.

Characterization of immune cell subphenotypes and activation status

To determine the effect of LPS on immune cell activation, cells in the hFM_DEC chamber were treated with LPS for 24 h and analyzed using CyTOF. The workflow for cell phenotyping based on CyTOF is shown in Fig. 3A. Cells were stained on-chip with a panel of 20 metal-tagged Abs against cell surface markers and intracellular markers (Tables I, II). Cytoskeletal markers showed CD45$^+$ (red; immune cells) in the inner chamber along with vimentin$^+$ (green) hFM_DECs, while the outer chamber contained cytokeratin$^+$ (yellow) hFM_CTCs in both control and LPS-treated devices (Fig. 3B). To visualize CyTOF data on a two-dimensional scatterplot, *t*-SNE was used, where immune cells with similar surface and intracellular marker expressions were grouped together. To determine the phenotypic diversity of immune cell populations on-chip within the two groups (i.e., control devices, inside+outside chambers; LPS devices, inside+outside chambers), a *k*-nearest neighbor density-based clustering algorithm called PhenoGraph (47) was conducted and overlaid on the *t*-SNE plot (Fig. 3C). To visualize the subphenotypes of cell populations, PhenoGraph information was used to create heatmaps to determine the relative intensity of each parameter for a given cluster (Supplemental Fig. 3). Cell clusters identified in the LPS-treated chips were normalized to control samples to determine the increase in immune cell abundance or activation of immune subtypes (Fig. 3D).

Our CyTOF analysis revealed a distinct increase (blue) in multiple activated immune cell populations within the LPS-treated chip compared with the control (Fig. 3D). Data presented in a heatmap, directed by the number of positive cells in the raw data, showed an increase in cell clusters characterized by 1) CD56$^+$, CD3$^-$, CD16$^+$, 2) CD16$^+$, CD25$^+$, CD11c$^+$, IL-17a$^+$, 3) HLA-DR$^+$, CD16$^+$, and 4) CD66b$^+$, CD16$^+$, IL-17a$^+$, IL-4$^+$. The expression pattern is consistent with cytotoxic NK cells, activated NK cells, neutrophils, and activated neutrophils, respectively. Interestingly, other populations with low frequency expressing either CD16$^+$, CD25$^+$, CD11c$^+$, or CD8a$^+$ in the LPS-treated group compared with the controls were also present. Although further characterization is needed, these markers are indicative of nonproinflammatory cytokine (i.e., IL-4, IL-17a, INF-γ)–producing activated NK cells and T cells, respectively. Taken together, our data determined the ability of LPS to shift the immune cell phenotype and induce immune cell activation at the FMi and showed that such phenomena are detectable using the dual-chamber choriodecidual interface MPS model.

FMi crosstalk during infectious conditions

Concentrations of pro- and anti-inflammatory cytokines, IL-8 and IL-10, respectively, as well as hormone (P4) and immunoregulatory factors (sHLA-G) were measured in both chambers after 24 h to determine whether LPS-induced immune cell migration and activation produced an inflammatory response to chorion compromise. We also determined whether the infectious environment remained localized to the maternal chamber or whether it elicited a response on the fetal side (Fig. 4). LPS treatment of the hFM_DEC chamber increased IL-8 production in the hFM_DEC chamber within 24 h (814 ± 324 pg/ml) compared

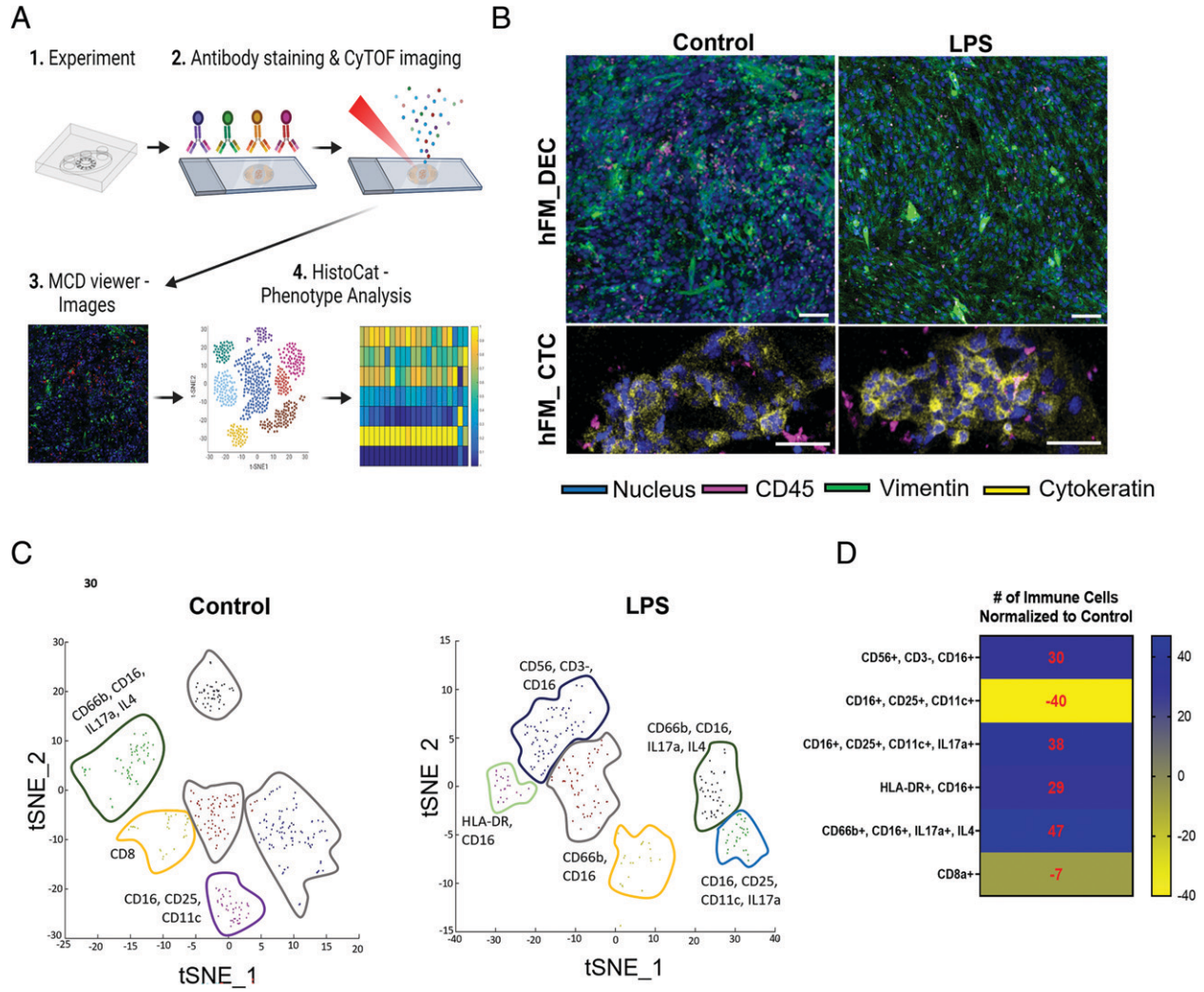

FIGURE 3. Imaging CyTOF analysis of immune cell subpopulations on-chip. (**A**) Illustration documenting the workflow of on-chip Ab staining and CyTOF image analysis. Created with BioRender. (**B**) CyTOF images showing vimentin$^+$ decidual cells (hFM_DECs; green) and CD45$^+$ leukocytes in the inner chamber (pink). Migratory leukocytes were identified by their CD45 staining in the chorion (hFM_CTC) chamber. Chorion cells in the outer chamber were only stained with cytokeratin (yellow). Scale bars, 100 μm. (**C**) Phenographs overlaid on *t*-SNE plots showing the specific immune cell clusters identified in each group (i.e., control devices, inside+outside chambers; LPS devices, inside+outside chambers). Different colors represent different histoCAT-identified cell clusters. Gray outlines represent clusters that did not meet the inclusion criteria. (**D**) Heatmap representing the normalized number of immune cells within specific clusters identified from imaging CyTOF (control versus LPS). Blue shows an increase in the immune cell population, and yellow shows a decrease.

with control (180 ± 75 pg/ml; $p = 0.04$) but not in the hFM_CTC chamber (Fig. 4A). Production of the anti-inflammatory cytokine IL-10 was not affected in either cell chamber (Fig. 4B). Additionally, LPS treatment to the maternal side resulted in significant changes in the hFM_CTC chamber, increasing the production of anti-inflammatory hormone P4 (control, 728 ± 234 pg/ml; LPS, 1794 ± 473 pg/ml; $p = 0.04$) (Fig. 4C) and immune regulator sHLA-G compared with controls (control, 94 ± 35 pg/ml; LPS, 186 ± 29 pg/ml; $p = 0.04$) (Fig. 4D). These data show that the experimental conditions employed in this study indicate that maternal- and fetal-specific responses of choriodecidual cells maintain homeostasis under infectious and inflammatory conditions. Of note, although not significant, chorion showed a trend in increasing IL-8 and decreasing IL-10 after LPS treatment, suggesting that increasing the dose of LPS, or time of incubation or even the power of sample size, may have produced a significant change. This trend is indicative of an expected immunocompromise at the interface, which will require further studies.

Table I. Immune cell profiles

Leukocytes	CD45$^+$		
M2 macrophages	CD45$^+$, CD68$^+$, CD206$^+$		
M1 macrophages	CD45$^+$, CD68$^+$, CD86$^+$/CD80$^+$		
NK cells	CD45$^+$, CD56$^+$/CD16$^+$/CD3-		
Dendritic cells	CD45$^+$, CD11c$^+$, HLA-DR$^+$		
Neutrophils	CD45$^+$, CD15$^+$/CD66B$^+$		
B lymphocytes	CD45$^+$, CD19$^+$		
T lymphocytes	Tregs	CD45$^+$, CD3$^+$, CD4$^+$, CD25$^+$	
	Th	CD45$^+$, CD3$^+$, CD4$^+$	
		Th1	CD45$^+$, INF-1
		Th2	CD45$^+$, IL-4
		Th17	CD45$^+$, IL-17
	CTLs	CD45$^+$, CD3$^+$, CD8$^+$	

Treg, regulatory T cell.

Discussion

Immune dysfunction during pregnancy at the choriodecidual interface is characterized by infiltration of activated inflammation-inducing immune cells into the fetal membrane (e.g., chorioamnion membrane) (2, 14, 48). This inflammatory response overrides the feto–maternal immune tolerance at this interface that maintains a healthy pregnancy (1, 2, 49–51), thus promoting the development of

Table II. Imaging mass cytometry Abs

Target Cells	Tagged Ab Description	Target	Label	Clone	Specificities	Source	Catalog No.
Chorion trophoblast cells (outer chamber)	Cytokeratin 154Sm	Cytokeratin (pan)	154Sm	C-11	All	BioLegend	628602
Decidual cells (inner chamber)	Vimentin 165Ho	Vimentin	165Ho	Polyclonal	Hu	R&D Systems	AF2105
Immune cells	CD3 170Er (MDA)	CD3	170Er	UCHT1	Hu	BioLegend	300443
	CD4 161Dy	CD4	161Dy	RPA-T4	Hu, Ch	BioLegend	300502
	CD25 149Sm	CD25	149Sm	2A3	Hu	DVS-Fluidigm	3149010B
	CD45 89Y	CD45	89Y	HI30	Hu, Ch	DVS-Fluidigm	3089003B
	CD8a 146Nd	CD8a	146Nd	RPA-T8	Hu	DVS-Fluidigm	3146001B
	HLA-DR 174Yb (MDA)	HLA-DR	174Yb	L243	Hu, Ch, Cy, Rh, Cn	BioLegend	307602
	CD11c 150Nd	CD11c	150Nd	Bu15	Hu	BioLegend	337221
	IFN-γ 158Gd	IFN-γ	158Gd	B27	Hu, Mk, Rh, Ch	DVS-Fluidigm	3158017B
	IL-17A 148Nd	IL-17A	148Nd	BL168	Hu	DVS-Fluidigm	3148008B
	CD68 171Yb	CD68	171Yb	Y1/82A	Hu	DVS-Fluidigm	3171011B
	CD80 162Dy	CD80	162Dy	2D10.4	Hu, Rh	DVS-Fluidigm	3162010B
	IL-4 142Nd	IL-4	142Nd	MP4-25D2	Hu	DVS-Fluidigm	3142002B
	CD19 163Dy	CD19	163Dy	HIB19	Hu, Ch	BioLegend	302202
	CD66b 143Nd	CD66b	143Nd	G10F5	Hu, Ch	BioLegend	305102
	CD206 168Er	CD206, MMR	168Er	15-2	Hu	DVS-Fluidigm	3168008B
	CD56 176Yb (DVS-NCAM16.2)	CD56	176Yb	NCAM16.2	Hu, Cy, Rh	DVS-Fluidigm	3176
	CD86 156Gd	CD86	156Gd	IT2.2	Hu	DVS-Fluidigm	3156008B
	CD16 209Bi	CD16	209Bi	3G8	Hu, Rh	DVS-Fluidigm	3209002B

chorioamnionitis that can lead to preterm birth (52–55). In this study, we investigated intercellular interactions between the choriodecidual immune interface and the differential cellular response by each cell type to an infectious stimulus. Principal findings of this study are as follows: 1) the developed MPS model is ideal for studying choriodecidual FMi immune homeostasis (we also report that primary immune cells isolated from human decidua parietalis can be seeded along with decidual cells, and their viability is maintained throughout the culture period, making it ideal to study the choriodecidual interface); 2) infection increases cytokine production, along with a reduction in HLA-DR expression, in decidual cells; 3) infectious stimulus on the maternal side causes immune cell migration toward the fetal side and 4) induces a shift in immune cell subpopulations and activation status across the choriodecidual interface; 5) the influx of decidual immune cells toward chorion trophoblasts (chorionitis) is associated with maternal inflammatory imbalance (cytokine changes); 6) chorion trophoblast HLA-G expression is not impacted by maternal LPS treatment or immune cell infiltration; and 7) chorion trophoblasts resist immune imbalance (i.e., generate tolerance) by enhancing an anti-inflammatory environment (an increase in P4 and sHLA-G), which could be a momentary trend. A tendency to downregulate IL-10 along with an increase in IL-8 and no change in immunomodulatory HLA-G on the chorion side is suggestive of a shift toward its collapse (Fig. 5). Infection load and type of infectious agent, its immunogenicity, and increased time of exposure to said agent may compromise chorion's functional integrity.

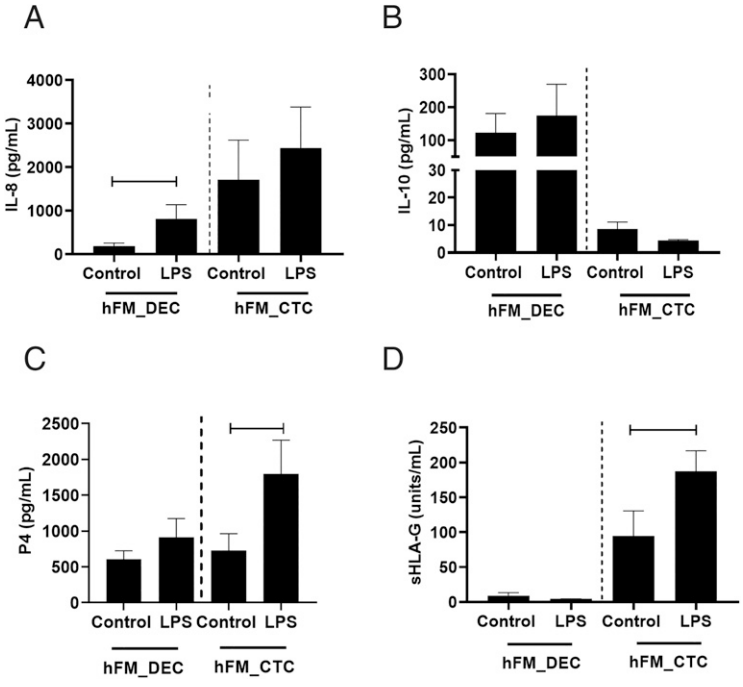

FIGURE 4. Maternal infection-induced inflammatory and hormonal changes at the choriodecidual immune interface. (**A** and **B**) Multiplex analysis measured supernatant concentrations of proinflammatory cytokine IL-8 and anti-inflammatory cytokine IL-10 in the inner and outer chamber after 24-h treatment. Maternal LPS treatment induced a significant increase in IL-8 production in decidual cells ($p = 0.04$) but did not affect IL-8 production in the chorion. Anti-inflammatory cytokine IL-10 levels did not change in either chamber regardless of treatment. Data are shown as mean ± SEM ($n = 5$). (**C** and **D**) ELISA measured media concentrations of anti-inflammatory hormone, progesterone (P4), and immune regulatory Ag, soluble HLA-G (sHLA-G), in the inner and outer chamber after 24-h treatment. Maternal LPS treatment induced a significant increase in P4 and sHLA-G production in chorion cells (P4, $p = 0.04$; sHLA-G, $p = 0.04$) but did not affect production in the decidua chamber compared with controls. Data are shown as mean ± SEM ($n = 5$).

In summary, our data indicate that immune homeostasis at the choriodecidual interface is maintained by constitutive expression of chorionic HLA-G and the anti-inflammatory properties of P4 and IL-10. HLA-G and sHLA-G likely protect the interface from immune cell infiltration. These protective mechanisms may be compromised in response to infection exposure, as seen with LPS stimulation in the presented study. The dose of LPS used in this study produced an immune cell influx and did not affect HLA-G in the chorion, suggesting that HLA-G or sHLA-G required to resist immune cell infiltration may not be available if infection persists. During the 24-h experimental period, chorion cells tend to withstand LPS stimulation with P4; however, it is unclear whether the P4 function is exclusively anti-inflammatory, as it is also involved in minimizing cellular transitions that can change trophoblasts into proinflammatory stromal cells. It is unlikely that the scenario observed in our study will persist when immune cell migration increases over time, leading to enhancement of the fetal inflammatory response that can eventually compromise the barrier integrity (Fig. 5). Cellular infiltration leading to chorioamnionitis is the first step, and subsequent inflammatory amplification can cause either rupture or membrane dysfunction leading to preterm birth.

During normal pregnancy, HLA-G and sHLA-G (a cleaved fragment from membrane HLA-G) (56) in the chorion trophoblasts and HLA-DR in the decidua modulate infiltration of immune cells and inhibit their cytotoxic and inflammatory effects (35, 57–61). These HLAs (i.e., HLA-G and HLA-DR) regulate decidual immune cell populations that are comprised of T cells (~36%), NK cells (~32%), macrophages (~16%), B cells (~5%), and neutrophils (~1%) (62–67) during gestation by 1) shifting T cells to a Th2 phenotype, 2) inducing NK senescence and inhibition of cytotoxic function, 3) preventing maturation of dendritic cells, 4) inhibiting B cell proliferation, 5) polarizing macrophages to an M2 phenotype, and 6) inducing phagocytosis and inhibiting reactive oxygen species production in neutrophils (59, 60, 68). We postulate that HLA-G expression and adequate production of sHLA-G are two main components of the chorion barrier that are critical for the structural and functional integrity of this region during pregnancy.

This study determined multiple parameters that can compromise immune homeostasis leading to a collapse of the interfaces' integrity during infection. We hypothesize that this occurs in three phases. In phase 1, infection and the spread of inflammation compromise the HLA barriers. In our model, LPS decreased HLA-DR expression in the decidua-CD45$^+$ coculture but did not change HLA-G expression in the chorion, suggesting that maternal infection can compromise the quiescent state of resident immune cells, prime their activation, and allow their migration into the chorion that does not contain high levels of HLA-G. Although maternal infection increased sHLA-G production in the chorion, this response is not sustainable without a similar increase in membrane-bound HLA-G, suggesting that chorion-induced tolerance to inflammation is short-lived. In phase 2—immune cell infiltration—changes in HLA-G can reduce choriodecidual defenses, prompting decidual immune cell infiltration. As seen in our CyTOF analysis, maternal infection also induces changes in the immunophenotype of cells by increasing the number of activated immune cells and by decreasing the number of quiescent cells. These changes can create an inflammatory environment. In phase 3—the spread of inflammation—when countering maternal proinflammatory cytokine and immune cell infiltration, the chorion may try to develop tolerance or succumb to the proinflammatory environment and collapse. As mentioned above, the fate of the interface and chorion's response is likely stimulant type-, dose-, and time-dependent. The consequence of the interface is difficult to draw from our studies, as the approach is limited to 24-h treatment of a single dose of LPS. However, we devised a model and demonstrated parameters that can determine the collapse or resilience of the choriodecidual interface.

The use of traditional two-dimensional cultures and animal models has failed to capture the complexities of human pregnancy and has been unsuccessful in understanding immune imbalances at the FMi. To overcome these limitations, this study adapts a previously validated two-chamber MPS device (38, 44, 69) to model immune regulation at the choriodecidual interface. Primary immune cells isolated from the decidua parietalis were cultured on-chip for 24 h to model the subpopulations of CD45$^+$ leukocytes present at the FMi (e.g., ~66% T cells, ~13% NK cells, ~4% macrophages, ~4% B cells, ~1.2% neutrophils). To our knowledge, this is the first time decidua-derived primary immune cells were cocultured in an MPS device, highlighting the novelty of these experiments. Additionally, infection-induced cell–cell communication, cell migration, and the subsequent response from the receiving end is not possible to emulate in a traditional culture system. Besides, inflammatory mediators diffusing through the microchannels between the choriodecidual chambers, mimicking paracrine interactions as expected in utero, is also replicated in this study. However, the kinetics of biochemical flow between the chambers and their functional impact are beyond the scope of this study. Therefore, we presume that such interactive

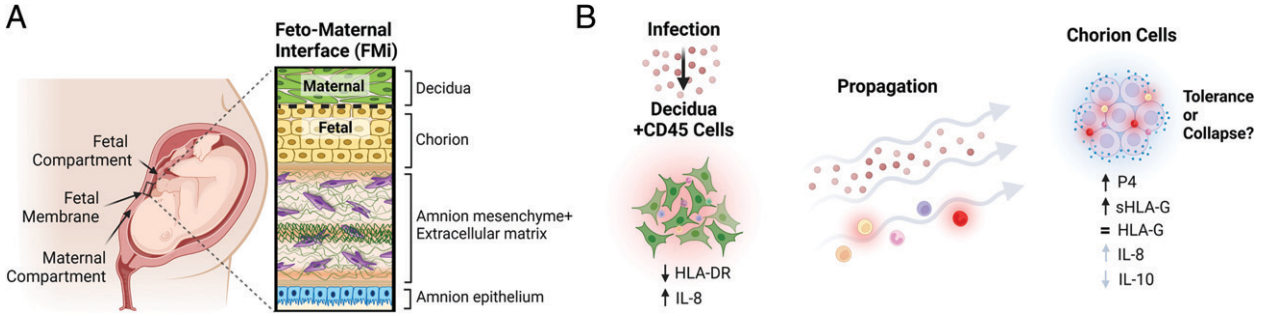

FIGURE 5. Infection-induced crosstalk at the choriodecidual immune interface. (**A**) Cartoon representing the feto–maternal interface during pregnancy. This interface is composed of maternal decidual cells connected to fetal-derived chorion trophoblast, amnion mesenchymal cells, and amnion epithelial cells. This interface forms at the choriodecidual junction, which is an immune cell barrier during normal pregnancy. (**B**) Schematic showing the crosstalk between the maternal decidual cells, immune cells, and fetal chorion during the presence of maternal infection and inflammation. Maternal infection induces decidua dysfunction by reducing the expression of immunoregulatory Ag HLA-DR and by increasing the production of proinflammatory cytokine IL-8. This inflammatory imbalance activates resident CD45$^+$ cells and promotes their migration into the chorion layer. Propagation of infection and CD45$^+$ cells is countered by chorion cells' production of 1) anti-inflammatory hormone, progesterone (P4), 2) immune neutralization factor, sHLA-G, 3) expression of membrane-bound HLA-G, and proinflammatory changes, including 4) an increasing trend of IL-8, and 5) no change in IL-10 production. These results suggest that infectious conditions can induce chorion cell tolerance, leading to pregnancy homeostasis, or induce chorion layer collapse, leading to ascending infection.

features that are normally expected in an organ's environment are successfully recreated in our MPS model, which are lacking in traditional culture systems.

Although this model has several advantages over current in vitro and in vivo systems (i.e., compared with transwells or coculture cell plates that are commercially available, the present model includes organ-on-a-chip data, a high signal-to-noise ratio [70], and it allows for visualization of migrating cells in real time [46]), it also contains limitations regarding experimental setup and endpoint analysis. Although primary immune cells are ideal to incorporate into this MPS, they exhibit a short half-life in vitro (~48 h) (Supplemental Fig. 2D, 2E) that inhibits long-term experiments, and nonadherent immune cell populations are lost before endpoint staining. Immune cell lines should be investigated for their utility (e.g., differentiation protocols and long-term viability) and capacity to recreate FMi immune phenotypes (i.e., marker expression) during pregnancy. Future studies will be conducted to develop a comprehensive and long-term MPS model of the choriodecidual immune interface. This will be accomplished by mechanistic chorion barrier studies and the adaptation of immune cells derived from cell lines to model the ratio of $CD45^+$ leukocyte phenotypes during gestation. These advancements will produce a robust in vitro model to study the complex cell–cell communication at the FMi and to delineate the interconnected role of the innate and adaptive immune system during gestation, term, and preterm labor.

Acknowledgments

We thank the Fluidigm company representatives that helped establish pipelines in CellProfiler and histoCAT for CyTOF data analysis.

Disclosures

The authors have no financial conflicts of interest.

References

1. Saito, S., A. Nakashima, S. Myojo-Higuma, and A. Shiozaki. 2008. The balance between cytotoxic NK cells and regulatory NK cells in human pregnancy. [Published erratum appears in 2008 *J. Reprod. Immunol.* 78: 84.] *J. Reprod. Immunol.* 77: 14–22.
2. Williams, P. J., R. F. Searle, S. C. Robson, B. A. Innes, and J. N. Bulmer. 2009. Decidual leucocyte populations in early to late gestation normal human pregnancy. *J. Reprod. Immunol.* 82: 24–31.
3. Bulmer, J. N., P. J. Williams, and G. E. Lash. 2010. Immune cells in the placental bed. *Int. J. Dev. Biol.* 54: 281–294.
4. PrabhuDas, M., E. Bonney, K. Caron, S. Dey, A. Erlebacher, A. Fazleabas, S. Fisher, T. Golos, M. Matzuk, J. M. McCune, et al. 2015. Immune mechanisms at the maternal-fetal interface: perspectives and challenges. *Nat. Immunol.* 16: 328–334.
5. Behnia, F., B. D. Taylor, M. Woodson, M. Kacerovsky, H. Hawkins, S. J. Fortunato, G. R. Saade, and R. Menon. 2015. Chorioamniotic membrane senescence: a signal for parturition? *Am. J. Obstet. Gynecol.* 213: 359.e1–359.e16.
6. Mor, G., and V. Abrahams. 2014. The immunology of pregnancy. In *Creasy & Resnik's Maternal-Fetal Medicine: Principles and Practice*, Chap 6, 7th Ed. R. K. Creasy, R. Resnik, J. D. Iams, C. L. Lockwood, T. R. Moore, and M. Greene, eds. Elsevier/Saunders, Philadelphia, p. 80–92.
7. Menon, R., E. A. Bonney, J. Condon, S. Mesiano, and R. N. Taylor. 2016. Novel concepts on pregnancy clocks and alarms: redundancy and synergy in human parturition. *Hum. Reprod. Update* 22: 535–560.
8. Menon, R. 2014. Oxidative stress damage as a detrimental factor in preterm birth pathology. *Front. Immunol.* 5: 567.
9. Joyce, E. M., J. J. Moore, and M. S. Sacks. 2009. Biomechanics of the fetal membrane prior to mechanical failure: review and implications. *Eur. J. Obstet. Gynecol. Reprod. Biol.* 144(Suppl. 1): S121–S127.
10. Sheller-Miller, S., E. Radnaa, J. K. Yoo, E. Kim, K. Choi, Y. Kim, Y. N. Kim, L. Richardson, C. Choi, and R. Menon. 2021. Exosomal delivery of NF-κB inhibitor delays LPS-induced preterm birth and modulates fetal immune cell profile in mouse models. *Sci. Adv.* 7: eabd3865.
11. Warning, J. C., S. A. McCracken, and J. M. Morris. 2011. A balancing act: mechanisms by which the fetus avoids rejection by the maternal immune system. *Reproduction* 141: 715–724.
12. Jacobs, S. O., S. Sheller-Miller, L. S. Richardson, R. Urrabaz-Garza, E. Radnaa, and R. Menon. 2021. Characterizing the immune cell population in the human fetal membrane. *Am. J. Reprod. Immunol.* 85: e13368.
13. Slutsky, R., R. Romero, Y. Xu, J. Galaz, D. Miller, B. Done, A. L. Tarca, S. Gregor, S. S. Hassan, Y. Leng, and N. Gomez-Lopez. 2019. Exhausted and senescent T cells at the maternal-fetal interface in preterm and term labor. *J. Immunol. Res.* 2019: 3128010.
14. Gomez-Lopez, N., D. StLouis, M. A. Lehr, E. N. Sanchez-Rodriguez, and M. Arenas-Hernandez. 2014. Immune cells in term and preterm labor. *Cell. Mol. Immunol.* 11: 571–581.
15. Menon, R., M. R. Torloni, C. Voltolini, M. Torricelli, M. Merialdi, A. P. Betrán, M. Widmer, T. Allen, I. Davydova, Z. Khodjaeva, et al. 2011. Biomarkers of spontaneous preterm birth: an overview of the literature in the last four decades. *Reprod. Sci.* 18: 1046–1070.
16. Saade, G. R., K. A. Boggess, S. A. Sullivan, G. R. Markenson, J. D. Iams, D. V. Coonrod, L. M. Pereira, M. S. Esplin, L. M. Cousins, G. K. Lam, et al. 2016. Development and validation of a spontaneous preterm delivery predictor in asymptomatic women. *Am. J. Obstet. Gynecol.* 214: 633.e1–633.e24.
17. Cantonwine, D. E., Z. Zhang, K. Rosenblatt, K. S. Goudy, R. C. Doss, A. M. Ezrin, G. Page, B. Brohman, and T. F. McElrath. 2016. Evaluation of proteomic biomarkers associated with circulating microparticles as an effective means to stratify the risk of spontaneous preterm birth. *Am. J. Obstet. Gynecol.* 214: 631.e1–631.e11.
18. Velez, D. R., S. J. Fortunato, N. Morgan, T. L. Edwards, S. J. Lombardi, S. M. Williams, and R. Menon. 2008. Patterns of cytokine profiles differ with pregnancy outcome and ethnicity. *Hum. Reprod.* 23: 1902–1909.
19. Parker, M. G., F. Ouyang, C. Pearson, M. W. Gillman, M. B. Belfort, X. Hong, G. Wang, L. Heffner, B. Zuckerman, and X. Wang. 2014. Prepregnancy body mass index and risk of preterm birth: association heterogeneity by preterm subgroups. *BMC Pregnancy Childbirth* 14: 153.
20. Babizhayev, M. A., and Y. E. Yegorov. 2011. Smoking and health: association between telomere length and factors impacting on human disease, quality of life and life span in a large population-based cohort under the effect of smoking duration. *Fundam. Clin. Pharmacol.* 25: 425–442.
21. Li, X., J. Zhou, M. Fang, and B. Yu. 2020. Pregnancy immune tolerance at the maternal-fetal interface. *Int. Rev. Immunol.* 39: 247–263.
22. Ander, S. E., M. S. Diamond, and C. B. Coyne. 2019. Immune responses at the maternal-fetal interface. *Sci. Immunol.* 4: eaat6114.
23. Vento-Tormo, R., M. Efremova, R. A. Botting, M. Y. Turco, M. Vento-Tormo, K. B. Meyer, J. E. Park, E. Stephenson, K. Polański, A. Goncalves, et al. 2018. Single-cell reconstruction of the early maternal-fetal interface in humans. *Nature* 563: 347–353.
24. Toothaker, J. M., P. Presicce, M. Cappelletti, S. F. Stras, C. C. McCourt, C. A. Chougnet, S. G. Kallapur, and L. Konnikova. 2020. Immune cells in the placental villi contribute to intra-amniotic inflammation. *Front. Immunol.* 11: 866.
25. Kim, C. J., R. Romero, P. Chaemsaithong, and J. S. Kim. 2015. Chronic inflammation of the placenta: definition, classification, pathogenesis, and clinical significance. *Am. J. Obstet. Gynecol.* 213(4 Suppl.): S53–S69.
26. Toothaker, J. M., O. Olaloye, B. T. McCourt, C. C. McCourt, T. N. Silva, R. M. Case, P. Liu, D. Yimlamai, G. Tseng, and L. Konnikova. 2022. Immune landscape of human placental villi using single-cell analysis. *Development* 149: dev200013.
27. Menon, R., N. N. Nicolau, S. Bredson, and J. Polettini, 2015. Fetal membranes: potential source of preterm birth biomarkers. In *General Methods in Biomarker Research and Their Applications.* V. R. Preedy and V. B. Patel, eds. Springer, Dordrecht, the Netherlands, p. 483–529.
28. Polettini, J., F. Behnia, B. D. Taylor, G. R. Saade, R. N. Taylor, and R. Menon. 2015. Telomere fragment induced amnion cell senescence: a contributor to parturition? *PLoS One* 10: e0137188.
29. Duchesne, M. J., H. Thaler-Dao, and A. C. de Paulet. 1978. Prostaglandin synthesis in human placenta and fetal membranes. *Prostaglandins* 15: 19–42.
30. Malak, T. M., C. D. Ockleford, S. C. Bell, R. Dalgleish, N. Bright, and J. Macvicar. 1993. Confocal immunofluorescence localization of collagen types I, III, IV, V and VI and their ultrastructural organization in term human fetal membranes. *Placenta* 14: 385–406.
31. Fortunato, S. J., R. Menon, K. F. Swan, and T. W. Lyden. 1994. Organ culture of amniochorionic membrane in vitro. *Am. J. Reprod. Immunol.* 32: 184–187.
32. Malak, T. M., and S. C. Bell. 1994. Structural characteristics of term human fetal membranes: a novel zone of extreme morphological alteration within the rupture site. *Br. J. Obstet. Gynaecol.* 101: 375–386.
33. El Khwad, M., B. Stetzer, R. M. Moore, D. Kumar, B. Mercer, S. Arikat, R. W. Redline, J. M. Mansour, and J. J. Moore. 2005. Term human fetal membranes have a weak zone overlying the lower uterine pole and cervix before onset of labor. *Biol. Reprod.* 72: 720–726.
34. Faas, M. M., and P. de Vos. 2017. Uterine NK cells and macrophages in pregnancy. *Placenta* 56: 44–52.
35. Sutton, L., D. Y. Mason, and C. W. Redman. 1983. HLA-DR positive cells in the human placenta. *Immunology* 49: 103–112.
36. Lozovyy, V., L. Richardson, G. Saade, and R. Menon. 2021. Progesterone receptor membrane components: key regulators of fetal membrane integrity. *Biol. Reprod.* 104: 445–456.
37. Richardson, L., S. Kim, R. Menon, and A. Han. 2020. Organ-on-chip technology: the future of feto-maternal interface research? *Front. Physiol.* 11: 715.
38. Richardson, L., S. Jeong, S. Kim, A. Han, and R. Menon. 2019. Amnion membrane organ-on-chip: an innovative approach to study cellular interactions. *FASEB J.* 33: 8945–8960.

39. Megli, C., and C. B. Coyne. 2021. Gatekeepers of the fetus: characterization of placental macrophages. *J. Exp. Med.* 218: e20202071.
40. Menon, R., E. Radnaa, F. Behnia, and R. Urrabaz-Garza. 2020. Isolation and characterization human chorion membrane trophoblast and mesenchymal cells. *Placenta* 101: 139–146.
41. Jin, J., L. Richardson, S. Sheller-Miller, N. Zhong, and R. Menon. 2018. Oxidative stress induces p38MAPK-dependent senescence in the feto-maternal interface cells. *Placenta* 67: 15–23.
42. Sheller, S., J. Papaconstantinou, R. Urrabaz-Garza, L. Richardson, G. Saade, C. Salomon, and R. Menon. 2016. Amnion-epithelial-cell-derived exosomes demonstrate physiologic state of cell under oxidative stress. *PLoS One* 11: e0157614.
43. Radnaa, E., R. Urrabaz-Garza, N. D. Elrod, M. Castro Silva, R. Pyles, A. Han, and R. Menon. 2022. Generation and characterization of human fetal membrane and decidual cell lines for reproductive biology experiments. *Biol. Reprod.* 106: 568–582.
44. Tantengco, O. A. G., L. S. Richardson, P. M. B. Medina, A. Han, and R. Menon. 2021. Organ-on-chip of the cervical epithelial layer: a platform to study normal and pathological cellular remodeling of the cervix. *FASEB J.* 35: e21463.
45. Dixon, C. L., L. Richardson, S. Sheller-Miller, G. Saade, and R. Menon. 2018. A distinct mechanism of senescence activation in amnion epithelial cells by infection, inflammation, and oxidative stress. *Am. J. Reprod. Immunol.* DOI: 10.1111/aji.12790.
46. Richardson, L., S. Jeong, S. Kim, A. Han, and R. Menon. 2019. Amnion membrane organ-on-chip: an innovative approach to study cellular interactions. *FASEB J.* 33: 8945–8960.
47. Im, I., Y. S. Son, K. B. Jung, I. Kang, B. E. Teh, K. B. Lee, M. Y. Son, and J. Kim. 2019. Mass cytometry-based single-cell analysis of human stem cell reprogramming uncovers differential regulation of specific pluripotency markers. *J. Biol. Chem.* 294: 18547–18556.
48. Yang, F., Q. Zheng, and L. Jin. 2019. Dynamic function and composition changes of immune cells during normal and pathological pregnancy at the maternal-fetal interface. *Front. Immunol.* 10: 2317.
49. Yin, F., Y. Zhu, M. Zhang, H. Yu, W. Chen, and J. Qin. 2019. A 3D human placenta-on-a-chip model to probe nanoparticle exposure at the placental barrier. *Toxicol. In Vitro* 54: 105–113.
50. Mori, M., A. Bogdan, T. Balassa, T. Csabai, and J. Szekeres-Bartho. 2016. The decidua-the maternal bed embracing the embryo-maintains the pregnancy. *Semin. Immunopathol.* 38: 635–649.
51. Feyaerts, D., M. Benner, B. van Cranenbroek, O. W. H. van der Heijden, I. Joosten, and R. G. van der Molen. 2017. Human uterine lymphocytes acquire a more experienced and tolerogenic phenotype during pregnancy. *Sci. Rep.* 7: 2884.
52. Zaidi, H., N. Lamalmi, L. Lahlou, M. Slaoui, A. Barkat, S. Alamrani, and Z. Alhamany. 2020. Clinical predictive factors of histological chorioamnionitis: case-control study. *Heliyon* 6: e05698.
53. Sagay, A. S. 2016. Histological chorioamnionitis. *J. West. Afr. Coll. Surg.* 6: x–xiii.
54. Romero, R., J. Espinoza, L. F. Gonçalves, J. P. Kusanovic, L. A. Friel, and J. K. Nien. 2006. Inflammation in preterm and term labour and delivery. *Semin. Fetal Neonatal Med.* 11: 317–326.
55. Romero, R., J. Espinoza, L. F. Gonçalves, J. P. Kusanovic, L. Friel, and S. Hassan. 2007. The role of inflammation and infection in preterm birth. *Semin. Reprod. Med.* 25: 21–39.
56. Rizzo, R., A. Trentini, D. Bortolotti, M. C. Manfrinato, A. Rotola, M. Castellazzi, L. Melchiorri, D. Di Luca, F. Dallocchio, E. Fainardi, and T. Bellini. 2013. Matrix metalloproteinase-2 (MMP-2) generates soluble HLA-G1 by cell surface proteolytic shedding. *Mol. Cell. Biochem.* 381: 243–255.
57. Le Bouteiller, P. 2015. HLA-G in human early pregnancy: control of uterine immune cell activation and likely vascular remodeling. *Biomed. J.* 38: 32–38.
58. da Silva, I. L., L. Montero-Montero, E. Ferreira, and M. Quintanilla. 2018. New insights into the role of Qa-2 and HLA-G non-classical MHC-I complexes in malignancy. *Front. Immunol.* 9: 2894.
59. Xu, H.-H., W.-H. Yan, and A. Lin. 2020. The role of HLA-G in human papillomavirus infections and cervical carcinogenesis. *Front. Immunol.* 11: 1349.
60. Loustau, M., F. Anna, R. Dréan, M. Lecomte, P. Langlade-Demoyen, and J. Caumartin. 2020. HLA-G neo-expression on tumors. *Front. Immunol.* 11: 1685.
61. Tantengco, O. A. G., L. Richardson, A. Lee, A. Kammala, M. C. Silva, H. Shahin, S. Sheller-Miller, and R. Menon. 2021. Histocompatibility antigen, class I, G (HLA-G)'s role during pregnancy and parturition: a systematic review of the literature. *Life (Basel)* 11: 1061.
62. Shah, N. M., P. F. Lai, N. Imami, and M. R. Johnson. 2019. Progesterone-related immune modulation of pregnancy and labor. *Front. Endocrinol. (Lausanne)* 10: 198.
63. Norwitz, E. R., P. M. Starkey, A. López Bernal, and A. C. Turnbull. 1991. Identification by flow cytometry of the prostaglandin-producing cell populations of term human decidua. *J. Endocrinol.* 131: 327–334.
64. Singh, U., G. Nicholson, B. C. Urban, I. L. Sargent, U. Kishore, and A. L. Bernal. 2005. Immunological properties of human decidual macrophages–a possible role in intrauterine immunity. *Reproduction* 129: 631–637.
65. Sindram-Trujillo, A. P., S. A. Scherjon, P. P. van Hulst-van Miert, H. H. Kanhai, D. L. Roelen, and F. H. Claas. 2004. Comparison of decidual leukocytes following spontaneous vaginal delivery and elective cesarean section in uncomplicated human term pregnancy. *J. Reprod. Immunol.* 62: 125–137.
66. Galazka, K., L. Wicherek, K. Pityński, J. Kijowski, K. Zajac, W. Bednarek, M. Dutsch-Wicherek, K. Rytlewski, J. Kalinka, A. Basta, and M. Majka. 2009. Changes in the subpopulation of $CD25^+$ $CD4^+$ and $FOXP3^+$ regulatory T cells in decidua with respect to the progression of labor at term and the lack of analogical changes in the subpopulation of suppressive B7-H4 macrophages—a preliminary report. *Am. J. Reprod. Immunol.* 61: 136–146.
67. Rinaldi, S. F., S. Makieva, P. T. Saunders, A. G. Rossi, and J. E. Norman. 2017. Immune cell and transcriptomic analysis of the human decidua in term and preterm parturition. *Mol. Hum. Reprod.* 23: 708–724.
68. Carosella, E. D., P. Moreau, S. Aractingi, and N. Rouas-Freiss. 2001. HLA-G: a shield against inflammatory aggression. *Trends Immunol.* 22: 553–555.
69. Richardson, L., A. K. Kammala, S. Kim, A. Han, and R. Menon. 2022. Novel bench-to-bedside tools: feto-maternal interface organ-on-chip's. *Am. J. Obstet. Gynecol.* 226(1 Suppl.): S712.
70. Richardson, L., J. Gnecco, T. Ding, K. Osteen, L. M. Rogers, D. M. Aronoff, and R. Menon. 2019. Fetal membrane organ-on-chip: an innovative approach to study cellular interactions. *Reprod. Sci.* DOI: 10.1177/1933719119828084.